Available online at www.sciencedirect.com

ScienceDirect

Procedia Computer Science 00 (2019) 000–000

Procedia Computer Science

www.elsevier.com/locate/procedia

Second International Conference on Intelligent Computing in Data Sciences (ICDS 2018)

Explicit radial basis function collocation method for computing shallow water flows

Elmiloud Chaabelasri[a,b*], Mohammed Jeyar[a], Alistair G.L. Borthwick[c]

[a]*LME, Faculté des sciences,Univertsité Mohamed premier, Oujda, Morocco*
[b] *ENSA, BP 03, Ajdir Al-Hoceima,Univertsité Mohamed premier, Morocco*
[c]*School of Engineering, The University of Edinburgh, The King's Buildings, Edinburgh EH9 3JL, UK*

Abstract

A simple Explicit Radial Basis Function (RBF) is used to solve the shallow water equations (SWEs) for flows over irregular, frictional topography involving wetting and drying. At first we construct the MQ-RBF interpolation corresponding to space derivative operators. Next, we obtain numerical schemes to solve the SWEs, by using the gradient of the interpolant to approximate the spatial derivative of the differential equation and a third-order explicit Runge-Kutta scheme to approximate the temporal derivative of the differential equation. Then, we verify our scheme against several idealized one-dimensional numerical experiments including dam-break and open channel flows over non-uniform beds (involving shock wave behavior), and moving wet-dry fronts over irregular bed topography. Promising results are obtained.

Keywords: Radial basis function, Shallow water equations, Friction, Irregular bed, Wetting and drying;

1. Introduction

In the past two decades, many numerical schemes have been proposed based on non-linear conservation laws for the solution of the shallow water equations (SWEs). High-order, mesh-based numerical schemes, utilizing finite difference, finite element, and finite volume discretizations, have been developed to reduce the number of computational cells and minimize the computational time required to achieve results of sufficient accuracy. For example, significant developments have occurred in the implementation of approximate Riemann solvers, such as Roe, HLL, or HLLC schemes see e.g. [1,2,3,4,5 and 6]. Such solvers have become very popular for solving the SWEs. However, node connectivity is an important issue when applying mesh-based numerical schemes to

hydraulic problems. The accuracy and stability of such methods depend greatly on the quality of the mesh; in general this is not a trivial issue, particularly when the boundary geometry is complicated. In this optic, meshless methods can be viewed as a good alternative, noting the relative simplicity of their implementation. Development of robust meshless methods for the numerical solution of partial differential equations has attracted considerable interest over the past twenty years, see e.g [7,8 and 9] . In particular, Fedoseyev et al. [10] and Cheng et al. [11] have shown that meshless radial basis functions (RBFs) are attractive options because of the exponential convergence of certain RBFs. Various RBFs have been successfully applied to obtain accurate, efficient solutions of partial differential equations of engineering interest. This method has been applied to solve inviscid compressible flows [12], natural convection [13], heat conduction [14], three-dimensional incompressible viscous flows [15], long waves in shallow water [16], and the vibration analysis of membranes [17].

In this paper, we examine the application of multiquadric radial basis functions (MQ-RBFs) to the numerical solution of the shallow equations for problems involving wetting/drying over complicated, frictional bed topography. In the formulation of MQ-RBFs, the radial basis functions represented by the multiquadric functions $\sqrt{1+\varepsilon^2(x-x_i)^2}$ are employed as basis functions to compute weighting coefficients for space differential operators, over a global set of computational collocation points [18]. The friction term is included in the momentum equations, and discretized by a splitting implicit scheme [6]. A third-order Runge-Kutta algorithm is used for time integration [19].

It is known that the system of shallow water equations admits non-smooth solutions that may contain shocks, rarefaction waves, and, in the case of non-smooth bottom topography, also contain contact discontinuities. To perform properly, a numerical method must be nonlinearly stable, because linearly stable methods may develop large spurious oscillations and even blow up. To stabilize the proposed MQ-RBF model for slowly varying flows, as well as rapidly varying flows involving shocks or discontinuities such as dam-breaks and hydraulic jumps, an artificial viscosity technique is used, following [20]. Furthermore, to avoid numerical instability caused by negative water depth near wet/dry fronts, the local flow variables are modified, imposing zero discharge when the water height became very small. As a consequence, the present numerical scheme ensures preservation of non-negative water depth and there is no need to limit the fluxes during simulation.

The paper is organized as follows: Section 2 outlines the shallow water equations. Section 3 presents the general formulation of partial differential problem interpolation using MQ-RBFs. Section 4 describes the application of MQ-RBFs to generate the discrete form of shallow water equations. Details are given of the numerical methods used to represent the friction term and carry out time integration. Section 5 discusses validation and application of the method; several numerical experiments are carried out for previously published benchmark cases in order to confirm the potential of the proposed scheme. Section 6 summarizes the main findings.

2. Shallow water equations

The shallow water equations (SWEs) have wide applications in ocean and hydraulic engineering, in particular with regard to river, reservoir, and open channel flows. The SWEs are derived from the Navier-Stokes equations under the following simplifying assumptions. First, it is assumed that vertical accelerations are sufficiently small to be neglected and that the fluid is homogeneous; the velocity profile can therefore be considered uniform through the depth. For a fixed bathymetry $z_b = z_b(x)$ (see Fig. 1) and neglecting viscous and Coriolis effects, the one-dimensional shallow water equations, containing geometrical source terms due to the bottom and friction topography, can be written as

$$\begin{cases} \frac{\partial}{\partial t}(h)+\frac{\partial}{\partial x}(hu)=0 \\ \frac{\partial}{\partial t}(hu)+\frac{\partial}{\partial x}(hu^2+\frac{1}{2}gh^2)=-gh\frac{\partial}{\partial x}(z_b)-C_f\|u\|u \end{cases} \tag{1}$$

where $h = h(x,t)$is the water depth, $u = u(x,t)$is the depth-averaged velocity component and g is the acceleration due to gravity. The right hand side of the momentum equation comprises a bed slope term and a bed friction term (in which $C_f = gn^2 h^{-1/3}$, with n the Manning coefficient).

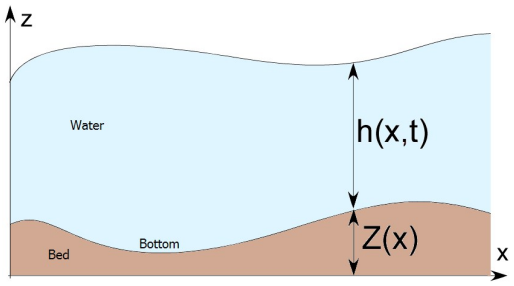

Fig. 1. Definition sketch for shallow water flow.

The system of shallow water equations is rewritten in a more compact form, as follows:

$$\frac{\partial}{\partial t} W + \frac{\partial}{\partial x} F(W) = S_z(W) + S_b(W) \tag{2}$$

where

$W = (h, hu)^T$;
$F(W) = (hu, hu^2 + 0.5gh^2)^T$;
$S_z(W) = (0, -gh\frac{\partial z}{\partial x})^T$ and
$S_b(W) = (0, -gn^2 \| u \| uh^{-1/3})^T$

Ignoring the right hand side, the system (2) reduces to a homogeneous hyperbolic system with real eigenvalues, $\lambda^- = u - \sqrt{gh}$ and $\lambda^+ = u - \sqrt{gh}$, and linearly independent eigenvectors.

3. The multiquadric radial basis function method

Let Ω be an open domain of $R^d, d=1;2$. Suppose $U = U(x,t)$ is a function to be approximated in a set of N pairwise distinct nodes $\mathbf{x} = \{x_1, x_2, ..., x_N\}$. In the RBF meshless scheme the approximation of U at the node x_i can be written as a linear combination of N RBFs

$$U(\boldsymbol{x},t) = \sum_{j=1}^{N} \lambda_j(t) \varphi(\| x - x_j \|, \varepsilon) \tag{3}$$

where $U(\mathbf{x},t) = [U(x_1,t), U(x_2,t), ..., U(x_N,t)]^T$ are the function values at node $\mathbf{x}$, $\Phi(\mathbf{x}) = [\varphi(\| x - x_1 \|, \varepsilon), \varphi(\| x - x_2 \|, \varepsilon), ..., \varphi(\| x - x_N \|, \varepsilon)]^T$ is a RBF centered at $\mathbf{x}$, $\| . \|$ denotes the Euclidean norm between nodes $\mathbf{x}$ and $\mathbf{x_j}$ and $\Lambda = [\lambda_1, \lambda_2, ..., \lambda_N]^T$ are coefficients to be determined.
One of the most commonly used RBFs is the multiquadric (MQ) RBFs [21]. Here we use the infinitely smooth multiquadric radial basis function defined as:

$$\varphi(\| x - x_j \|, \varepsilon) = \sqrt{1 + \varepsilon^2 (x - x_j)^2} \tag{4}$$

where ε is a shape parameter that controls the fit of a smooth surface to the data. In the present work we used the following selection [22]

$$\varepsilon = 0.8\frac{\sqrt{N}}{d_m} \tag{5}$$

in which d_m denotes the smallest nodal distance. The expansion coefficients Λ in (3) are obtained by solving the following linear system of $N \times N$ algebraic equations of $U(x_i,t) = U_i$

$$\Phi\Lambda = \boldsymbol{U} \tag{6}$$

the expansion coefficients are then calculated by

$$\Lambda = \Phi^{-1}\boldsymbol{U} \tag{7}$$

where $\mathbf{U} = \left[U_1, U_2, ..., U_N\right]^T$ is the vector of approximate solutions, $\Phi = (\varphi(\| x_i - x_j \|, \varepsilon))_{1 \le i,\, j \le N}$ is an $N \times N$ matrix of RBFs given as:

$$\begin{pmatrix} \varphi(\| x_1 - x_1 \|, \varepsilon) & \dots & \varphi(\| x1 - xN \|, \varepsilon) \\ \vdots & & \vdots \\ \varphi(\| x_N - x_1 \|, \varepsilon) & \dots & \varphi(\| x_N - x_N \|, \varepsilon) \end{pmatrix}_{N \times N}$$

Space derivatives of the interpolant (3) may be readily calculated, due to its linearity. Generally, the first and second-order spatial derivatives at the points $\boldsymbol{x}$ can be calculated as

$$\frac{\partial \boldsymbol{U}^{(k)}}{\partial x^k} = \sum_{j=1}^{N} \lambda_j(t) \frac{\partial \varphi^{(k)}}{\partial x^k}(\| x_i - x_j \|, \varepsilon) \tag{8}$$

in which k=(1,2) denotes first and second-order derivatives. In a compact matrix form, using equation (7), equation (8) can be written as

$$\frac{\partial \boldsymbol{U}^{(k)}}{\partial x^k} = \Phi_{x^{(k)}}\Lambda = \Phi_{x^{(k)}}\Phi\boldsymbol{U} \tag{9}$$

where

$$\frac{\partial \boldsymbol{U}^{(k)}}{\partial x^k} = \left[\frac{\partial U^{(k)}(x_1,t)}{\partial x^k}, \frac{\partial U^{(k)}(x_2,t)}{\partial x^k}, ..., \frac{\partial U^{(k)}(x_N,t)}{\partial x^k} \right]^T \tag{10}$$

and

$$\Phi_{x^{(k)}} = \left[\frac{\partial^{(k)}\Phi(x_1)}{\partial x^k}, \frac{\partial^{(k)}\Phi(x_2)}{\partial x^k}, ..., \frac{\partial^{(k)}\Phi(x_N)}{\partial x^k} \right]^T \tag{11}$$

4. Discretized form of SWEs by MQ-RBF

4.1. Convective flux and bottom topography term approximations

Let us assume that $F^n(\boldsymbol{U}(x))$ are known convective fluxes at time $t = n\Delta t$. Using (3), they can be approximated by

$$F^n(W) = \sum_{j=1}^{N} \lambda_j(t)\varphi(\| x - x_j \|, \varepsilon) \tag{12}$$

and in matrix form, these equations become

$$F^n = \Lambda^n \Phi \tag{13}$$

However, the expansion coefficients are then calculated by

$$\Lambda^n = \Phi^{-1} F^n \tag{14}$$

From (12), the partial flux derivative $\frac{\partial F^n(W)}{\partial x}$ can be written as:

$$\frac{\partial F^n(\boldsymbol{W})}{\partial x} = \sum_{j=1}^{N} \lambda_j^n(t) \frac{\partial \varphi(\| x - x_j \|, \varepsilon)}{\partial x} \tag{15}$$

Then, the compact matrix form of the partial derivative of the flux vector is:

$$\frac{\partial F^n(\boldsymbol{W})}{\partial x} = \Phi_x \Lambda^n = \Phi_x \Phi F^n(\boldsymbol{W}) \tag{16}$$

Applying the same procedure described above for the bottom topography function $z_b(x)$, it is easy to obtain its discrete form. The topography function can be approximated by

$$z_b^n(x) = \sum_{j=1}^{N} \alpha_j(t) \varphi(\|x - x_j\|, \varepsilon) \tag{17}$$

and its partial derivative is then expressed as,

$$\frac{\partial z_b^n(x)}{\partial x} = \sum_{j=1}^{N} \alpha_j(t) \frac{\partial \varphi(\|x - x_j\|, \varepsilon)}{\partial x} \tag{18}$$

In the same way, the compact matrix form of the bottom topography term $S_{z_b}^n$ is given as:

$$S_{z_b}^n = -gh^n \frac{\partial z_b^n(\mathbf{x}, t)}{\partial x} = -gh^n \Phi_x \Phi z_b^n(\mathbf{x}, t) \tag{19}$$

4.2. Addition of friction effects

To incorporate friction into the present numerical scheme, the friction term is discretized using an operator splitting procedure described in [23], which splits the shallow water equations (2) into two equations:

$$\begin{cases} \dfrac{\partial hu}{\partial t} = S_b^{n+1}(\boldsymbol{W}) = (-gn^2 \| u \| uh^{-1/3})^{n+1} \\ \dfrac{\partial hu}{\partial t} + \mathcal{L}(\boldsymbol{W}, Z_b) = 0 \end{cases} \tag{20}$$

In the first step of the calculation, the upper ordinary differential equation in (21) is approximated by an implicit method as [6]:

$$\frac{\overline{hu} - (hu)^n}{\Delta t} = S_b^{n+1} \tag{21}$$

where the friction term S_b^{n+1} may be expressed using a Taylor series as:

$$S_b^{n+1} = S_b^n + \left(\frac{\partial S_b}{\partial hu}\right)^n \left((\overline{hu}) - (hu)^n\right) + 0(\Delta(hu)^2) \tag{22}$$

Rearranging the above equation leads to the following formula for updating water discharge $\overline{hu}$ at the new time step

$$\overline{hu} = (hu)^n + \Delta t \frac{S_b^n}{1 + 2\Delta t C_f \| u \| h^{-1}} \tag{23}$$

In the second step, the value $\overline{hu}$ is taken to be the initial condition when solving the second equation in (21).

4.3. Time integration and stability condition

To date, the forward Euler method has been mainly used as the preferred time stepping scheme for RBF methods. However, the forward Euler method is only first-order accurate in time and so may introduce excessive numerical dissipation in the computed RBF solutions. To achieve a higher order of accuracy, we use the explicit Runge-Kutta method recommended by [19]. The procedure to advance the solution from the time t^n to the next time t^{n+1} is carried out as

$$\begin{aligned} \mathcal{W}^{(1)} &= \boldsymbol{W}^n + \Delta t \mathcal{L}(\boldsymbol{W}^n) \\ \mathcal{W}^{(2)} &= \frac{3}{4}\boldsymbol{W}^n + \frac{1}{4}\mathcal{W}^{(1)} + \frac{1}{4}\Delta t \mathcal{L}(\mathcal{W}^{(1)}) \\ \boldsymbol{W}^{n+1} &= \frac{1}{3}\boldsymbol{W}^n + \frac{2}{3}\mathcal{W}^{(2)} + \frac{2}{3}\Delta t \mathcal{L}(\mathcal{W}^{(2)}) \end{aligned} \tag{24}$$

where n represents the time level, and Δt is the time step. To achieve stability (for this explicit scheme) the time step must meet the following criterion:

$$\Delta t = CFL \frac{d_{\min}}{\max(\| u_i \| + \sqrt{g h_i})} \tag{25}$$

where the CFL is the Courant number, such that $0 < \mathrm{CFL} < 1$, and $d_{\min}$ denotes the smallest nodal distance between collocation points.

4.4. Boundary conditions

In this work, transmissive boundary conditions for open inflow/outflow and reflective boundary conditions for solid walls are applied in the simulations. At a transmissive boundary, the flow variables at a collocation point on the boundary are set to the same values as at the interior point normal to the boundary. At a reflective boundary, the value at a collocation point is simply the mirror image of that at the associated boundary point, so that the normal velocity component is zero at the boundary. However, the representation of boundary conditions within a MQ-RBF method is less trivial.

4.5. Artificial viscosity for shock-capturing

For particular hydraulic problems involving shock-waves, such as a hydraulic jump or dam-break flows, the numerical model is required to represent a steady or unsteady discontinuity, where the presence of oscillations in the solution is expected, and sometimes may grow over time. However, by introducing a small amount of artificial diffusion, it is possible to damp these oscillations [20 and 24]. We therefore augment the right hand side of the hyperbolic system (2) with the artificial diffusion term

$$\mathcal{D}(\boldsymbol{W}) = D_h \frac{\partial^2 \boldsymbol{W}}{\partial x^2} \tag{26}$$

where D_h is a tunable viscosity coefficient. The Peclet number is defined as follows:

$$P_e = \frac{max(\lambda_i^+, \lambda_i^-)}{D_h} d_{min} \tag{27}$$

and it often controls the stability of the numerical solutions [20 and 25]. In the case of convection-dominated flow, the Peclet number is large but finite, and the effect of the diffusion term (27) becomes negligible. Therefore, a natural and simple way to stabilize the solution is to reduce the Peclet number.
Using the RBFs interpolation of an arbitrary function (9), the augmented term (27) can be obtained as

$$\mathcal{D}(\mathbf{W}) = \frac{\max(\lambda_i^+, \lambda_i^-)}{P_e} d_{\min} \mathbf{\Phi}_{xx} \mathbf{\Phi} \mathbf{W} \cdot \tag{28}$$

5. Results and discussion

5.1. One-Dimensional Dam-Break Problems

5.1.1. Dam break over a wet bed

A one-dimensional dam break over a wet, horizontal bed is first simulated to demonstrate the shock-capturing capability of the corrected MQ-RBF method using artificial viscosity. The channel is of length 20 m. The initial water discharge and depth are given by:

$$hu(x,0) = 0 \text{ and } h(x,0) = \begin{cases} 10 & if \ x \le 10 \\ 2 & otherwise \end{cases} \tag{29}$$

As boundary conditions, a zero discharge and a free boundary are considered at the left and right ends of the channel. The analytical solution for this simple dam-break test consists of a backward-propagating rarefaction and a forward-moving shock wave. Fig. 2 shows the numerical results of flow after the dam fails, at three different times in terms of water surface elevation and discharge. Here, the model domain consists of 800 points. An artificial viscosity of 0.001 m2s-1 is applied corresponding to a Peclet number of 300. Figs 3 and 4 show close-up views of the evolving free surface elevation and discharge profiles along the channel at different times. In general, satisfactory agreement is achieved between the numerical and analytical solutions, although a very small amount Xof numerical diffusion occurs where the surface gradient is steepest.

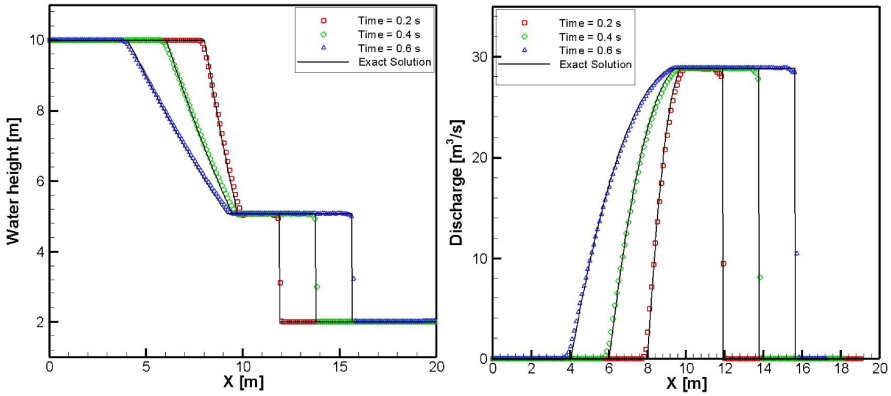

Fig. 2. Numerical and exact solutions of a dam break on a wet bed, at different times, using a grid of 800 points. Left: free surface elevation profiles; right: profiles of water discharge per unit breadth.

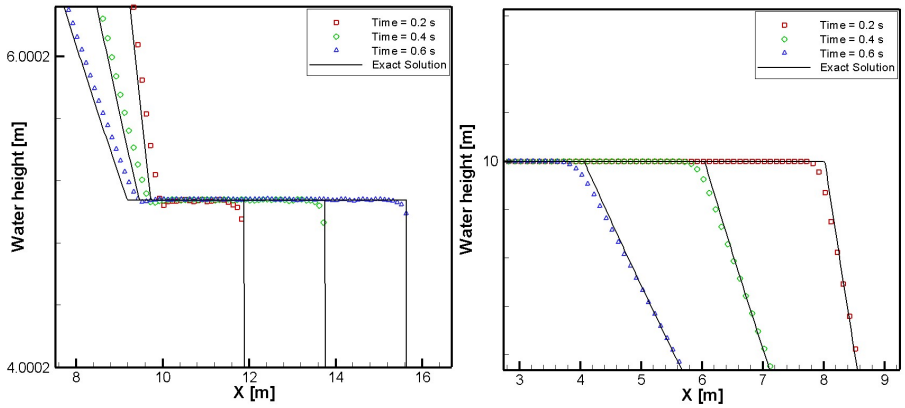

Fig. 3. Same as Fig. 2, zoom-in, focusing on discontinuities in water level.

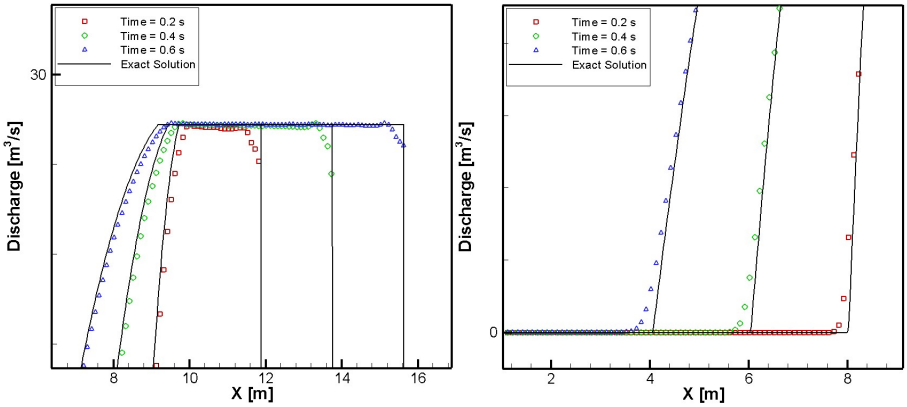

Fig. 4. Same as Fig. 2, zoom-in, focusing on discontinuities in discharge.

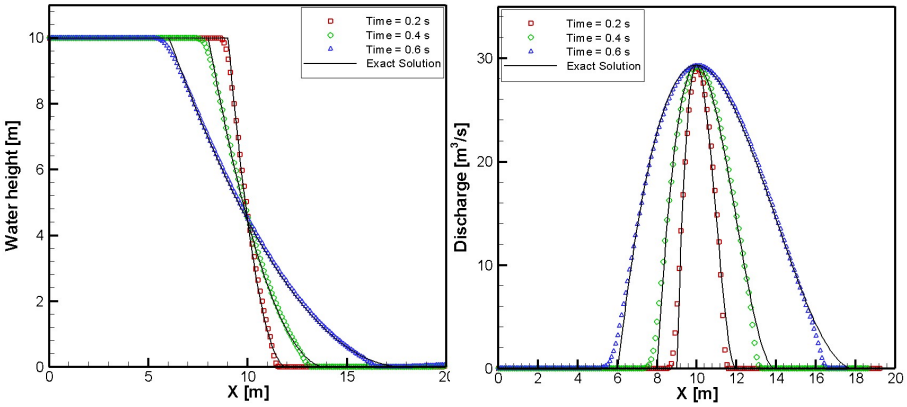

Fig. 5. Numerical and exact solutions for a dam break on a dry bed, at different times, using a grid with 800 points. Left: free surface elevation profiles; right: profiles of discharge per unit breadth.

5.1.2. Dam break over a dry bed

In this case, the previous wet bed dam-break test is modified to test the capability of the current MQ-RBFs in handling wet-dry fronts and small water depths. The previous initial conditions are modified to be

$$hu(x,0)=0 \text{ and } h(x,0)=\begin{cases}10 \ \ if \ \ x\le 10\\ 0 \ \ \ otherwise\end{cases} \tag{30}$$

i.e., an initial still water level on the left hand side of the dam at x = 10m, and a dry region on the right. In practice, the region is considered dry when the water depth is less than $\varepsilon = 10^{-6} m$. Zero discharge, $hu = 0$, is imposed at the left boundary at $x = 0$; and a free boundary condition is implemented at the right boundary $x = 20$ m. The domain is again discretized into 800 grid points, and the simulation carried out until $t = 0.6s$ after the dam instantaneously fails. The artificial viscosity is set to 0.001 m^2s^{-1}. Fig. 5 shows the numerical predictions. Again, the numerical predictions agree satisfactorily with the analytical solution. No additional treatment is needed to track the wet/dry front because the bed is flat and horizontal in this case.

5.2. Flow over a hump

To investigate the ability of the MQ-RBF algorithm to establish steady-state solutions, we apply the numerical solver to a series of benchmark test problems for subcritical, and transcritical flows. These problems are widely used to test numerical algorithms for the shallow-water equations, e.g. [26,27 and 28]. In these test examples the channel length is 25 m and the bottom topography $z_b(x)$ is defined as,

$$Z_b(x)=\begin{cases}0.2-0.05(x-10)^2 \ \ if \ \ 8\le x\le 12 \ \text{m}\\ 0 \ \ \ \ \ \ \ \ \ \ \ \ \ \ \ \ otherwise\end{cases} \tag{31}$$

with the initial water depth and discharge given by

$$h(x,0) \ = \ 2 \ - z_b(x) \ and \ \ hu(x,0) \ = \ 0 \ m^2 s^{-1} \tag{32}$$

Depending on the boundary conditions, the flow can be subcritical or transcritical, with or without a steady shock (hydraulic jump). All results are displayed at $t = 200s$ using a grid of 800 points, with CFL fixed at 0.6. Analytical solutions for the various cases are given by Goutal and Maurel [29] and Xing [27].

- Transcritical flow without a shock

The discharge is prescribed as hu = 1.53 m^2s^{-1} at the upstream inlet boundary, and the water depth is fixed as$h$ = 0.66 mat the downstream outlet boundary. Fig. 6 shows the close agreement between the predicted and analytical profiles of stage, $h + z_b$, and discharge, hu, along the channel. Slight discrepancies in discharge arise from sampling hu as a dependent variable, rather than as a flux [28]

- Transcritical flow with a shock

To develop a transcritical flow with a shock, the upstream discharge is set to 0.18 m^2s^{-1} and the downstream water depth to 0.33 m. In this case, the Froude number, $Fr=\sqrt{u/gh}$, increases to a value greater than unity above the hump as the flow becomes transcritical. Over the downstream face of the hump, a hydraulic jump occurs as a stationary surge wave (or hydraulic shock) downstream of which the flow becomes subcritical and the Froude number decreases to below unity. Fig. 7 plots stage and discharge profiles along the channel, with the hydraulic jump evident in the free surface profile. The numerical predictions are non-oscillatory and in satisfactory agreement with the corresponding analytical solutions.

- Subcritical flow

In this case, the prescribed upstream discharge is 4.42 m^2s^{-1} and the downstream depth is 2 m.. The flow is everywhere subcritical. Fig. 8 depicts the predicted stage and discharge profiles which are again in good agreement with the corresponding analytical solutions.

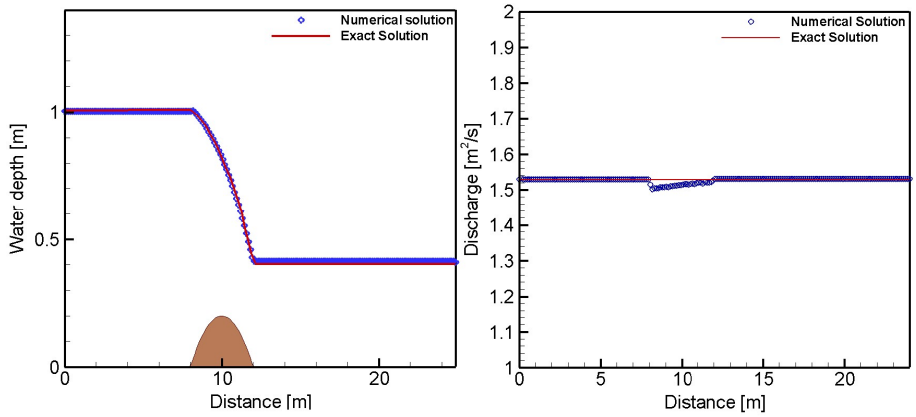

Fig. 6. Steady transcritical flow over a bed hump, without a shock: Predicted and analytical profiles of stage (left) and discharge per unit breadth (right); the topography is colored brown.

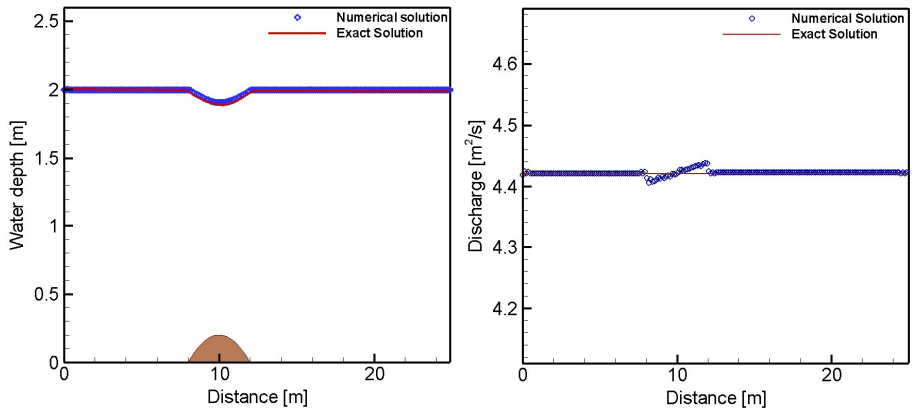

Fig. 7. . Steady transcritical flow over a bed hump, with a shock: Predicted and analytical profiles of stage (left) and discharge per unit breadth (right); the topography is colored brown.

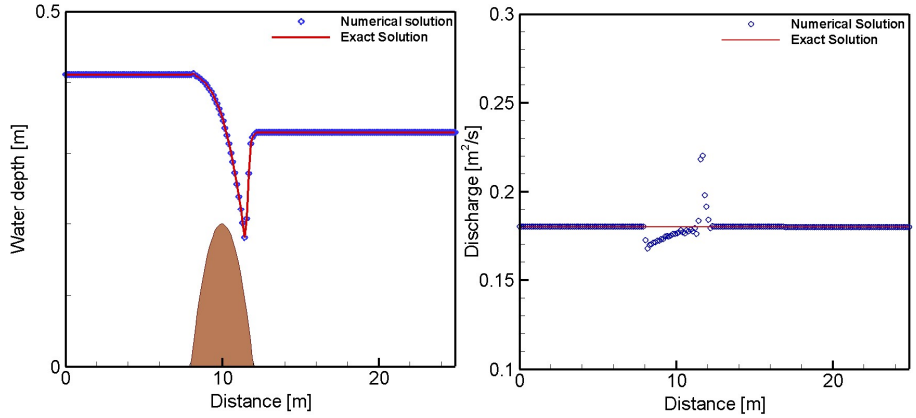

Fig. 8. . Steady subcritical flow over a bed hump: Predicted and analytical profiles of stage (left) and discharge per unit breadth (right); the topography is colored brown.

5.3. Drainage over a bed hump

A drainage problem where a dam break wave overtops a bed hump, and the downstream face dries out, is now used to test the ability of the proposed method to handle drying processes on a non-uniform bed. The problem was originally proposed by Gallouet et al. [30], and was also considered by Xing [27]. The flow is computed in a domain of length 38 m which contains a triangular hump on an otherwise flat bed. At the left boundary, a free condition is applied to the water depth h whereas the discharge is set to zero. At the right boundary, the depth and discharge are both set to zero, corresponding to a dry bed. Full details of the flow domain and parameters are given by Gallouet et al. [30].The bottom topography is given by

$$z_b(x) = \begin{cases} 0 & if\ x \le 25.5 \\ ax - ba & if\ 25.5 \le x \le 28.5\ \text{m} \\ -ax + (b+6)a & if\ 28.5 \le x \le 31.5 \\ 0 & if\ 31.5 \le x \end{cases} \quad (33)$$

where $a = 0.4/3$ and $b = 25.5$. The initial water height and discharge are

$$h(x,0)=0.75 - z_b(x) \quad \text{and} \quad hu(x,0) = 0\ . \quad (34)$$

The computational domain is discretized into 800 grid points, the CFL number is set to 0.6, and the simulation carried out for a total duration of 400 s. Fig. 9 shows the evolving stage profiles along the channel at times t = 0.5, 1.5, 3.5, and 400 s. The outlet boundary condition on the right allows the water to flow freely out of the domain on the right, and a dry region develops near the right side of the hump. After a long time, the solution reaches steady state, with still water to the left of the hump, and a dry bed to the right. The numerical solutions properly reproduce this pattern, and converge to the expected steady state.

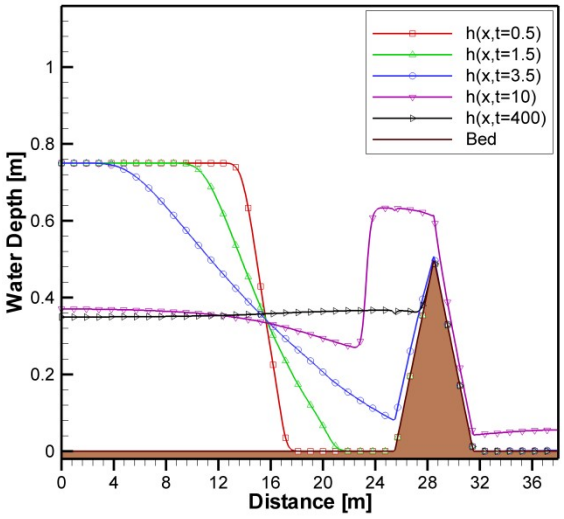

Fig. 9. Stage profiles at different times for dam break flow over a hump, where drainage occurs on the downstream slope of the hump.

5.4. Dam break flow over a triangular hump

In this test case, we examine the performance of the proposed scheme with a dam break wave over a triangular obstacle downstream of the dam. Fig. 10 shows the reservoir, channel and triangular obstacle geometry, along with the location of the measurement gauges. A reservoir containing water of initial depth 0.75m is connected to a rectangular channel with a symmetric triangular obstacle located downstream of the dam. The Manning roughness coefficient is n=0.0125 s.m$^{-1/3}$ throughout. The boundaries are solid walls except for the free outlet at the end of the

channel. Experimental data are reported by Shirkhania et al. [31] at gauge points G1,G2,G3,G4, and G5 which are located 4, 10, 11, 13, and 20m downstream of the reservoir. We compute the solution using MQ-RBFs with 800 grid points. In Fig. 11, we present the time evolution of the computed water depths at the gauge points and compare the predicted and measured values. For all gauges located upstream and downstream of the obstacle, the water depth and the arrival time of the wave are properly predicted, confirming the capability of the scheme to predict actual dam break flooding, albeit at laboratory scale.

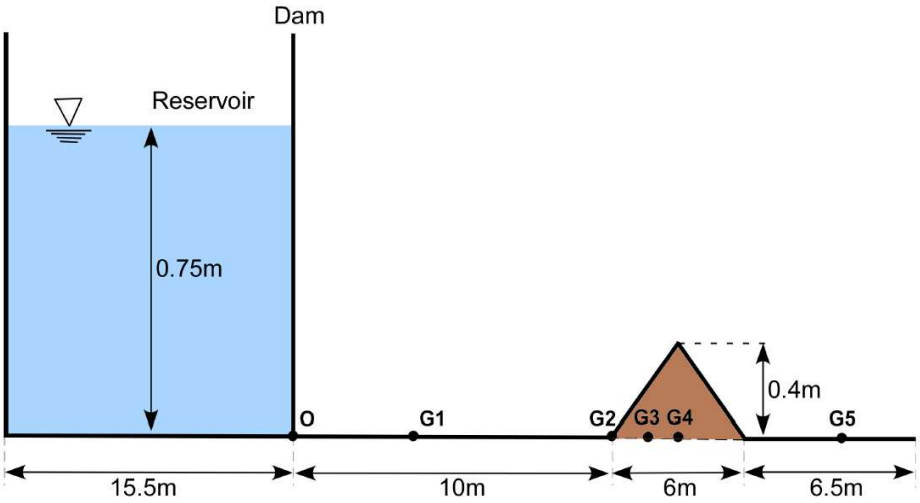

Fig. 10. Schematic side view of Shirkhania et al.'s (2016) experimental model showing gauge point locations, for dam break flow over a triangular hump.

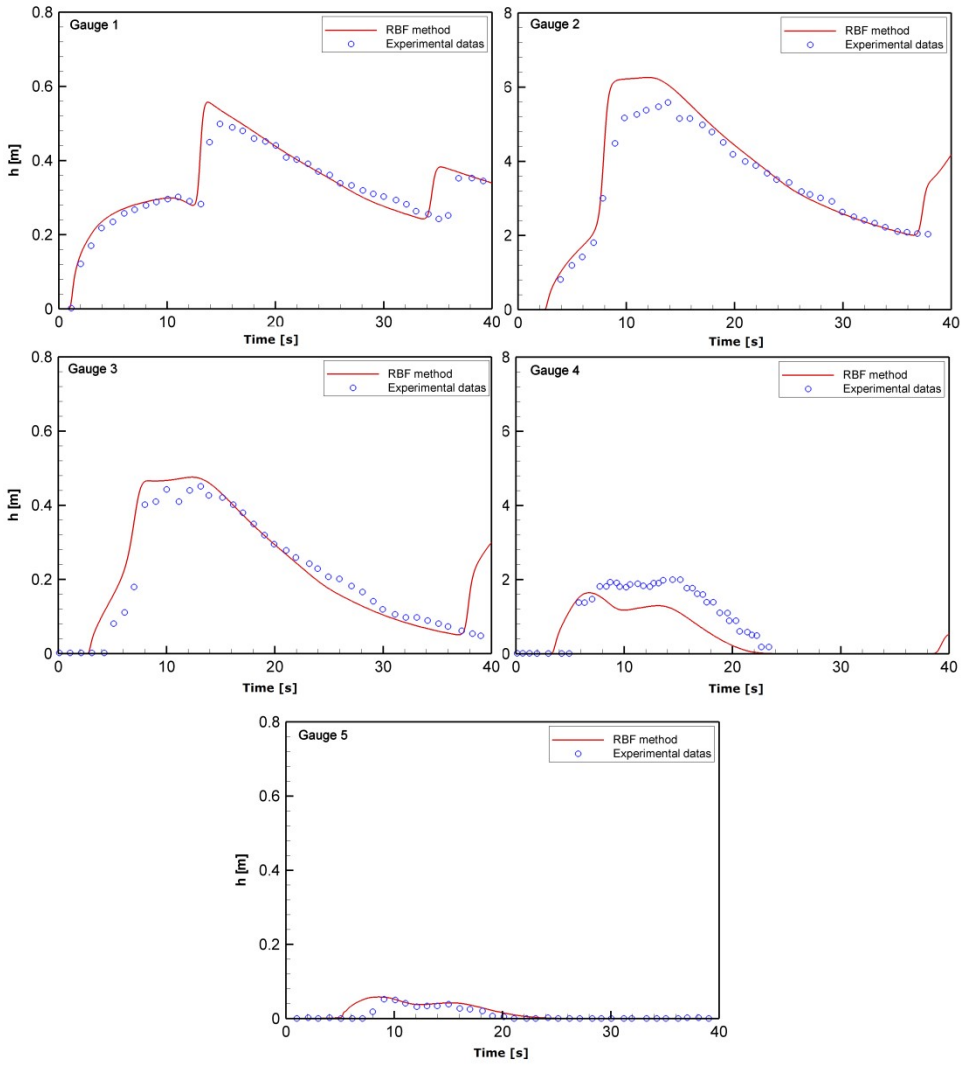

Fig. 11. Dam break over a triangular obstacle: predicted and measured water depthtime histories at gauging points G2, G4, G8, G10, G11, G13 and G20.

6. CONCLUSIONS

This paper has investigated a simple MQ-RBFs meshless method for solving the shallow water equations including bed friction and non-uniform bed elevation terms. The space derivative has been approximated by radial basis functions on global collocation points. An explicit 3rd order Runge-Kutta scheme was used for time integration. The MQ-RBFs meshless method has been found to be flexible and straightforward to implement. The method is particularly attractive in comparison with classical mesh-based methods because it is inherently mesh-free and requires no special treatment of the wet-dry interface. The method was tested against several standard benchmark problems. Excellent agreement was obtained between the numerical predictions and analytical solutions for one-dimensional dam break bore and rarefaction flows over wet and dry beds. The model was also tested for open channel flow over a bed hump, where again close agreement was achieved between the numerical predictions and analytical solutions of the stage-discharge profiles along the channel. A drainage test demonstrated the model properly reproduced drying processes over non-uniform bed topography. Finally, the method was applied to a

laboratory dam break over an initially dry bed with a triangular hump. The numerical model gives promising predictions by comparison with previously published experimental data.

References

[1] Leveque, R. (1998). Balancing source terms and flux gradients in high-resolution godunov-type methods. *J. Comput. Phys*. 146:346–365.

[2] Hubbard, M. and P. García-Navarro (2000). Flux difference splitting and the balancing of source terms and flux gradients. *J. Comput. Phys*. 165:89–125.

[3] Chaabelasri, E., N. Salhi, I. Elmahi. F. Benkhaldoun, Second order well balanced scheme for treatment of transcritical flow with topography on adaptive triangular mesh, International Journal of Physical and Chemical. News 53 (2010) 119-128.

[4] Brufau, P., P. Garcia-Navarro, and M. Vazquez- Cendon (2004). Zero mass error using unsteady wetting-drying conditions in shallow flows over dry irregular topography. *Int. J. Numer. Meth* 45: 1047–1082.

[5] Mohammadian, A. and D. LeRoux (2006). Simulation of shallow flows over variable topographies using unstructured grids. *Int. J. Numer. Meth* 52: 473–498.

[6] Kesserwani, G. and Q. Liang (2012). Locally limited and fully conserved RKDG shallow water solutions with wetting and drying. *J Sci Comput* 50:20–144.

[7] Belytschko, T., Y. Krongauz, D. Organ, M. Fleming,and P. Krysl (1996). Meshless methods: an overview and recent developments. *Comput Methods Appl Mech Eng* 139: 3–47.

[8] Liu, G. (2002). Mesh free methods: moving beyond the finite element method, Boca Raton, Fl: *CRCPress.*

[9] Nguyen, V., T. Rabczuk, S. Bordas, and M. Duflot (2008). Meshless methods: a review and computer implementation aspects. *Math Comput Simulat* 79: 763–813.

[10] Fedoseyev, A., M. Friedman, and E. Kansa (2002).Improved multiquadric method for elliptic partial differential equations via p-DE collocation on the boundary. *Comput Math Appl* 43:491–500.

[11] Cheng, A., M. Golberg, E. Kansa, and T. Zammito(2003). Exponential convergence and h-c multiquadric collocation method for partial differential equations. *Numer Meth PDEs*19:571–594.

[12] Shu, C., H. Ding, H. Chen, and T. Wang (2005). Anupwind local RBF-DQ method for simulation of inviscid compressible flows. *Comput Methods Appl Mech Eng* 194: 2001–2017.

[13] Ding, H., C. Shu, K. Yeo, and Z. Lu (2005). Simulation of natural convection in eccentric annuli between a square outer cylinder and a circular inner cylinder using local MQ-DQ method. *Numer Heat Appl* 47(3): 291–313.

[14] Soleimani, S., D. Ganji, E. Ghasemi, M. Jalaal, and H. Bararnia (2011). Meshless local RBF-DQ for 2-d heat conduction: a comparative study. *Therm Sci* 15: 117–121.

[15] Ding, H., C. Shu, K. Yeo, and D. Xu (2006). Numerical computation of three-dimensional incompressible viscous flows in the primitive variable form by local multiquadric differential quadrature method. *Comput Methods Appl Mech Eng* 195: 516–533.

[16] Khoshfetrat, A. and M. Abedini (2013). Numerical modeling of long waves in shallow water using LRBF-DQ and hybrid DQ//LRBF-DQ. *Ocean Model* 65:1–10.

[17] Wu, W., C. Shu, and C. Wang (2007). Vibration analysis of arbitrarily shaped membranes using localradial basis function-based differential quadrature method. *J Sound Vib*306: , 252–270.

[18] Kansa, E. (2007). Exact explicit time integration of hyperbolic partial differential equations with meshfree radial basis functions. *Engineering Analysis with Boundary Elements* 31:577–585.

[19] Ullrich, P., C. Jablonowski, and B. van Leer (2010).High-order finite-volume methods for the shallow water equations on the sphere. *Journal of Computational Physics* 229: 6104–6134.

[20] Stevens, D. and H. Power (2015). The radial basis function finite collocation approach for capturing sharp fronts in time dependent advection problems. *Journal of Computational Physics*,http://dx.doi.org/10.1016/j.jcp.2015.05.032.

[21] Sarra, S. (2006). Integrated multiquadric radial basis function approximation methods. *Computers & Mathematics with Applications* 51:1283–1296.

[22] Benkhaldouna, F., A. Halassi, D. Ouazar, M. Seaid,and A. Taik (2017). A stabilized meshless method for time-dependent convection-dominated flow problems. *Mathematics and Computers in Simulation* 137:159–176.

[23] Boushaba, F., E. Chaabelasri, N. Salhi, I. Elmahi, F. Benkhaldoun, and A. Borthwick (2008). Acomparative study of finite volume and finite element on some transcritical free surface flowproblems. *International Journal of Computational Methods* 5:413–431.

[24] Xia, X., Q. Liang, M. Pastor, W. Zou, and Y. Zhuang (2013). Balancing the source terms in a SPH model for solving the shallow water equations. *Advances in Water Resources* 59: 25–38.

[25] Jackson S.J, D. Stevens, D.Giddings, H.Power (2016) An adaptive RBF finite collocation approach to track transport processes across moving fronts, Comp. Math. With App. 71: 278–300

[26] Seaid M. (2004), Non-oscillatory relaxation methods for the shallow-water equations in one and two space dimensions, Int. J. Numer. Meth. Fluids; 46:457-484

[27] Xing, Y. (2016). High order finite volume WENO schemes for the shallow water flows through channels with irregular geometry. *Journal of Computational and Applied Mathematics* 299: 229–244.

[28] Ying, X and Wang S.S.Y. (2008). Improved implementation of the HLL approximate Riemann solver for one-dimensional open channel flows, *Journal of Hydraulic Research*, 46(1): 21-34.

[29] Goutal N., and Maurel F. (Eds.) (1997).*Proceedings of the 2nd Workshop on Dam-Break Wave Simulation*, HE 43/97/016/B, Département Laboratoire National d'Hydraulique, Groupe Hydraulique Fluviale Electricité de France, France.

[30] Gallouet, T., J. Herard, and N. Seguin (2003).Some approximate Godunov schemes to compute shallow-water equations with topography. *Computers& Fluids* 32:479–513.

[31] Shirkhania, H., A. Mohammadian, O. Seidou, andA. Kurganov (2016). A well balanced positivity preserving central upwind scheme for shallow water equations on unstructured quadrilateral grids.*Computers and Fluids* 126:25–40.